Research Article | Vol. 28, No. 13 / 22 June 2020 / Optics Express 18790
Optics EXPRESS

Fundamental limitations of spectrally-sliced optically enabled data converters arising from MLL timing jitter

ANDREA ZAZZI,[1] JULIANA MÜLLER,[1] SERGIY GUDYRIEV,[3] PABLO MARIN-PALOMO,[2] DENGYANG FANG,[2] J. CHRISTOPH SCHEYTT,[3] CHRISTIAN KOOS,[2] AND JEREMY WITZENS[1,*]

[1]*Institute of Integrated Photonics, RWTH Aachen University, Campus Blvd. 73, Aachen 52074, Germany*
[2]*Institute of Photonics and Quantum Electronics, Karlsruhe Institute of Technology, Engesserstrasse 5, 76131 Karlsruhe, Germany*
[3]*Heinz Nixdorf Institute, Paderborn University, Fürstenallee 11, 33102 Paderborn, Germany*
[*]*jwitzens@iph.rwth-aachen.de*

Abstract: The effect of phase noise introduced by optical sources in spectrally-sliced optically enabled DACs and ADCs is modeled and analyzed in detail. In both data converter architectures, a mode-locked laser is assumed to provide an optical comb whose lines are used to either synthesize or analyze individual spectral slices. While the optical phase noise of the central MLL line as well as of other optical carriers used in the analyzed system architectures have a minor impact on the system performance, the RF phase noise of the MLL fundamentally limits it. In particular, the corresponding jitter of the MLL pulse train is transferred almost one-to-one to the system-level timing jitter of the data converters. While MLL phase noise can in principle be tracked and removed by electronic signal processing, this results in electric oscillator phase noise replacing the MLL jitter and is not conducive in systems leveraging the ultra-low jitter of low-noise mode-locked lasers. Precise analytical models are derived and validated by detailed numerical simulations.

1. Introduction

The growing demand for high data rates poses tremendous challenges for high bandwidth electronic signal processing. With the advent of coherent optical communications and the pervasive use of digital signal processing, the performance requirements for digital-to-analog (DAC) and analog-to-digital (ADC) data converters have been rising, in terms of required analog bandwidth, sampling rate, as well as signal-to-noise ratio (SNR) and effective number of bits (ENOB). Current electronic data converters are limited by aperture jitter originating from electronic clock jitter, which results in a tradeoff between bandwidth and resolution [1].

State-of-the-art, oven-controlled quartz crystal oscillators (OCXOs) with a repetition rate of 100 MHz have a jitter in the order of a few tens of fs and a phase noise in the order of -135 dBc/Hz at 100 Hz frequency offset [2], resulting in a single-sideband (SSB) phase noise power spectral density (PSD) of -95 dBc/Hz when upconverted to a 10 GHz oscillation frequency [3], as required for high-speed data converters. In order to improve reference clock jitter, sapphire crystal microwave oscillators [4,5] running at a 10 GHz center frequency have been adopted, featuring phase noise as low as -130 dBc/Hz at 100 Hz offset [6].

Beyond the capabilities of purely electrical systems, optical pulse trains have been investigated as a means to generate lower jitter clocks. Best-in-class Ti:sapphire mode-locked lasers (MLLs) feature phase noise below -160 dBc/Hz at 100 Hz frequency offset, as also scaled up to a 10 GHz harmonic (repetition rate), resulting in jitter in the attosecond range [7]. These exceptionally low jitter levels have rekindled interest in using mixed electrical-optical signal processing not only as

#382832 https://doi.org/10.1364/OE.382832
Journal © 2020 Received 11 Nov 2019; revised 8 Mar 2020; accepted 14 Apr 2020; published 9 Jun 2020

Optics EXPRESS

a means to enable extremely broadband signal processing, but also to reach low jitter values and thus record-high ENOB in high-speed data converters [8].

Such extreme low jitter levels will be more challenging to achieve with semiconductor gain media, due to increased technical noise, but also because the phase noise of the generated pulse train scales with the square of the temporal pulse width [7], τ^2, limited by the width of the optical gain spectrum. However, a quantum dot (QD) semiconductor optical amplifier (SOA) embedded in a 6 meter fiber loop and actively mode-locked with a repetition frequency of 12.8 GHz has yielded a phase noise of -120 dBc/Hz at 100 Hz frequency offset [9], close to the performance of best-in-class sapphire oscillators. Since the optical spectrum of the MLL, at 2 nm, was still relatively narrow for a QD-based material, further improvement of the pulse train jitter characteristics should be achievable, motivating research on the integration of such light sources at the chip scale [10–13]. As a further chip-scale alternative, the on-chip integration of rare-earth gain media is also being pursued [14].

A number of concepts for optically enabled ADCs have been proposed [15], two examples of which – the time-interleaved and the spectrally-sliced ADC – are schematically represented in Fig. 1. While the objective of this paper is to analyze the fundamental jitter limitations of the spectrally-sliced ADC, both are briefly reviewed to enable a comparison. Time-stretch ADCs are a further architecture benefiting from low jitter MLLs [16].

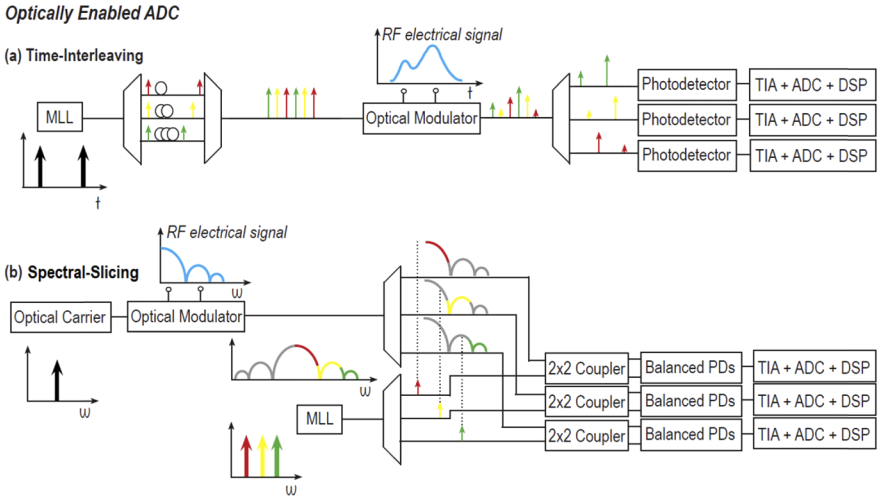

Fig. 1. Time-interleaved and spectrally-sliced ADC architectures. The time-interleaved architecture (a) utilizes frequency de/multiplexing and delay lines implementing differential group delays to generate a pulse train with higher repetition rate consisting of interleaved pulses with different center frequencies. In the spectrally-sliced architecture (b), spectral slices are individually analyzed by coherent receivers supplied with reference tones by an MLL, with the resulting information aggregated in the digital domain to recover the broadband signal.

In the time-interleaved ADC shown in Fig. 1(a) [8], a pulse train is first generated by an MLL with a repetition period T_r. The pulses are sent through a coarse wavelength division (WDM) demultiplexer (demux) with passbands much wider than the free spectral range (FSR) of the MLL. This results in the pulse train being split into N pulse trains each maintaining the initial pulse repetition rate, but whose spectra are centered at different frequencies. These pulse trains are delayed relative to each other in increments of T_r/N prior to being recombined by a WDM-mux into a single beam. This results in a sequence of N interleaved pulses of different center frequencies, spaced by T_r/N and repeating with an overall cycle period T_r. After

Optics EXPRESS

modulation of the signal onto this beam, the pulse trains are again separated according to pulse center frequency by means of a WDM-demux, prior to being sent to an array of N parallel photodetectors (PDs) and ADCs, each clocked at $1/N$ of the overall system sampling rate.

The 2nd method shown in Fig. 1(b), the spectrally-sliced ADC [17], is the one that will be analyzed in more details in the following. Here, an electric signal is directly amplitude modulated onto a continuous wave (CW) carrier and the resulting wideband optical signal subsequently spectrally-sliced into N channels using optical passband filters. Each spectral slice is independently analyzed by mixing it with an individual reference tone provided by a comb line from an MLL. After detection by a PD array and subsequent digitization, the slices are stitched back together by digital signal processing (DSP), to reconstruct the original signal. Further implementation-specific details will be given in Section 2.

For the time-interleaved architecture, the jitter of the pulse train generated by the MLL can be straightforwardly seen to map one-to-one to the system level jitter as reflected by the signal quality at the output of the optically enabled ADC. This mapping is however much less clear in the spectrally-sliced ADC, in which the signal is indirectly processed in the frequency domain. Since timing information must be ultimately provided by the MLL, one may intuit that here too the system is limited by the MLL's pulse train jitter – however, this remains to be verified. Another question arises regarding the tolerance of the system to other sources of optical noise, such as the phase noise of the carrier onto which the signal is being modulated. While individual slices rely on coherent (heterodyne) receiver subsystems, the system in its entirety is essentially a high-speed direct detection receiver, since the input signal is amplitude encoded onto the carrier and eventually retrieved after data aggregation. Thus, one may expect carrier phase noise to play less of a role, which will also be quantified in the following.

Similar considerations apply for DACs. Highly spectrally efficient modulation formats such as Nyquist pulse modulation, discrete multitone (DMT) or optical orthogonal frequency division multiplexing (OFDM) [18] require the generation of precise waveforms at increasing bandwidths and sampling rates. High-speed optical communication systems increasingly rely on software-programmable analog waveform generators implemented through DACs at the transmitter front-end [19]. State-of-the-art BiCMOS DACs reach analog bandwidths in excess of 40 GHz [20]. However, as state-of-the-art electro-optic modulators can reach bandwidths well in excess of 100 GHz [21–24], it will become increasingly difficult to precisely synthesize waveforms required to take full advantage of their electro-optic bandwidths. As for the optically enabled ADCs, joint electrical-optical signal processing allows breaking down the electric signal processing into several parallel channels with lower requirements.

A number of optically enabled DAC architectures have been developed, with time-interleaved [25–27] and spectrally-sliced [28] architectures in close analogy to the optically enabled ADCs described above. Here too, the jitter limitations of the spectrally-sliced DAC architecture shown in Fig. 2 warrants deeper analysis, also covered in the following.

The digital signal is first filtered by a series of filters with adjacent passbands, so as to slice it into several sub-channels in the frequency domain. These are then frequency down-converted, converted to the analog domain with reduced speed electronic DACs, and used to modulate individual comb lines of a previously frequency demultiplexed MLL with single-sided electro-optic modulation. The relative frequencies of the comb lines serve to upconvert the signal slices back, wherein the FSR of the MLL coincides with the passband width of the digital filters. The slices are multiplexed back together with a WDM-mux or a simple combiner (for reduced distortion) and the combined optical signal sent to a high-speed PD.

This paper evaluates the impact of optical noise sources on the performance of optically enabled, spectrally-sliced ADCs and DACs. These are evaluated both numerically, as well as with a compact analytical model, wherein numerical results serve to verify and validate the latter. The paper is structured as follows: In Section 2, we give a more detailed description of the optically

Optics EXPRESS

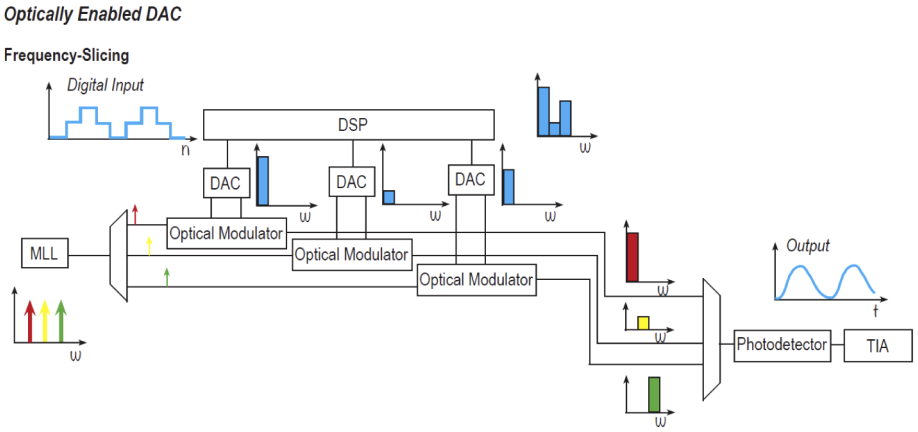

Fig. 2. Optically enabled DAC relying on spectral slicing. A DSP passband filters and down-converts individual signal slices before sending them to lower speed electric DACs and single-sided electro-optic modulators. Optical carriers are provided in the form of filtered comb lines sourced by an MLL whose FSR coincides with the passband width of the digital filters. After recombining the slices in the optical domain, the resulting optical signal is sent to a high-speed PD regenerating the converted signal in the analog domain.

enabled spectrally-sliced ADC architecture, including some implementation-specific details. A model for the optically enabled ADC is derived in Section 3, with a focus on laser phase noise. In Section 4, we discuss the numerical results in regards to optical phase noise and MLL pulse jitter. An analytical model for the prediction of system performance is derived and validated with the numerical results. Section 5 applies this analysis to the spectrally-sliced DAC, deriving similar analytical formulas for the latter by closely following prior derivations. Finally, Section 6 discusses the ENOB achievable with existing MLLs as predicted by the models. An outlook on ongoing developments is given in the conclusions.

2. Proposed system architecture

This section gives more details on the architecture of the spectrally-sliced ADC shown in Fig. 1(b), also taking into account constraints arising from a reduction to practice in the silicon electronic-photonic integrated circuit (ePIC) technology of the Leibniz Institute for Innovative Microelectronics (IHP).

Spectral-slicing allows transferring some of the signal processing challenges from the optical to the digital domain. For instance, in a time-interleaved ADC dispersion introduced by optical waveguides must be dealt with in the optical domain, since the architecture is dependent on maintaining narrow pulses. In a spectrally-sliced ADC, on the other hand, dispersion compensation can be handled in the electrical domain by means of digital signal processing, as explained in the following. Handling of dispersion with digital electronics rather than with optical components has proven very beneficial in other application fields, such as coherent communications. This is of particular relevance when integrating the optically enabled ADC and DAC architectures, due to the dispersion associated to fibers and on-chip waveguides. Moreover, spectrally-sliced ADCs have been much less investigated than time-interleaved ones, and are not as well understood, which is in and by itself an important motivation for this investigation.

The described architecture is based on four 30 GHz slices, yielding a total bandwidth of 120 GHz. Its modularity allows straightforwardly increasing the bandwidth by adding more slices, for example by using several 4-channel chips in parallel, each covering a different 120 GHz range and receiving a portion of the (re-amplified) light exiting the modulator. The maximum

Optics EXPRESS

achievable bandwidth is thus ultimately limited by the bandwidth of the electro-optic modulator, the width of the MLL spectrum, and the noise budget of the system.

The details of the architecture and its reduction to practice are illustrated in Fig. 3. The electric signal that is to be digitized is first converted to the optical domain with the help of a single-frequency laser and a broadband electro-optic modulator [21–24]. The modulator is a Mach-Zehnder modulator biased at its quadrature point that is amplitude modulating the RF signal onto the optical carrier. While this creates a double-sided optical spectrum, only one half of the spectrum is analyzed, since this suffices to retrieve the entire information. While single-sided modulation could have been employed instead to obtain a better optical power budget, this would require preprocessing the electric signal and thus its prior digitization with the jitter associated to an electric oscillator – defeating the very reason an optically enabled digitization scheme is used here. Beyond distortion (that can be compensated), discarding one of the signal side-bands also impacts the noise performance of the system (see Section 4).

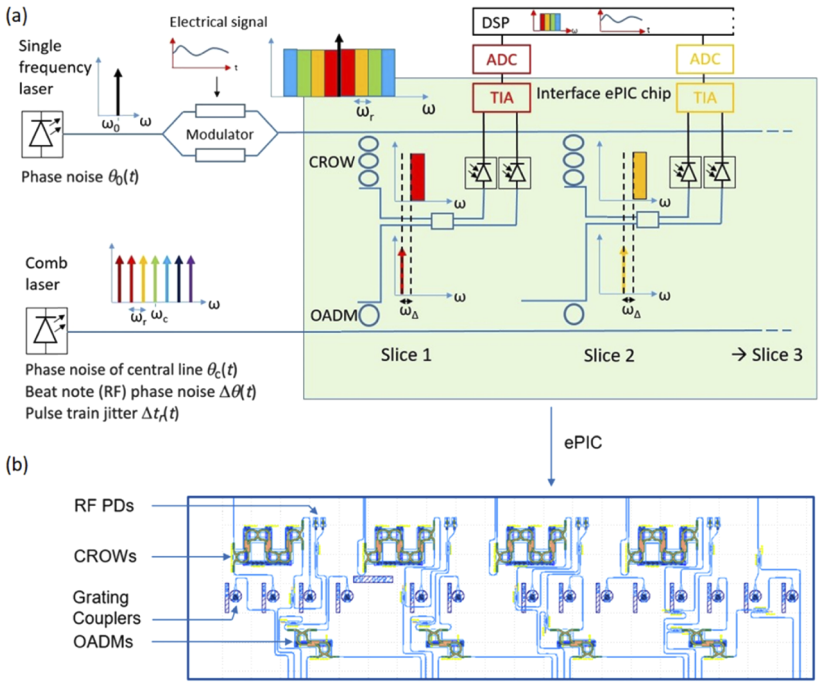

Fig. 3. (a) Detailed schematic of the proposed architecture, implementing a spectrally-sliced optically enabled ADC in a silicon ePIC. A single frequency laser serves as carrier onto which the RF signal is applied. The modulated signal is spectrally sliced into multiple channels by means of 3rd order CROW filters operated in drop configuration and analyzed by heterodyne coherent receivers each using a different MLL line as reference tone. The green area represents the set of functionalities implemented on the ePIC. (b) Layout of the optical part of the developed ePIC.

The modulated optical signal is coupled to an electronic-photonic integrated circuit (ePIC), in which it is sliced into 4 channels by 3rd order coupled-resonator optical waveguide (CROW) filters [29,30] with a passband ω_r that matches the FSR of the MLL. The CROW filters approximate square shaped transfer functions with 3rd order Chebyshev filters, with sufficient spectral overlap between the slices to enable phase error estimation and stitching between slices during digital post-processing [17]. MLL comb lines are dropped by optical add-drop multiplexers (OADM) consisting of single rings [31], since here a flat-top passband is not required. The signal

Optics EXPRESS

slice and the MLL reference tone are sent to the two input ports of a 2-by-2 3-dB directional combiner-splitter (DCS) followed by a balanced pair of high-speed germanium waveguide PDs [32] amplified by a differential transimpedance amplifier (TIA) [33], digitally postprocessed and aggregated with data from the other slices (Section 3).

In [17], each slice was coherently detected by choosing the frequency of the reference tone to be in the center of the slice's passband (intradyne detection). This effectively doubles the frequency range that can be covered per slice, as limited by the speed of the electronics, as both signal frequencies above and below the reference tone can be detected. However, this also requires the implementation of a 90-degree hybrid as well as two balanced PD pairs and differential TIAs per channel. We have rather opted for heterodyne detection with the frequency of the reference tone provided by the MLL slightly below the lower edge of the sliced signal passband. Since only positive beat-note frequencies are detected, a 90-degree hybrid is no longer required and can be replaced by a simple DCS. Moreover, while the spectral range is restricted to positive beat-notes and thus halved, the amount of circuitry per slice is also halved as only a single PD pair and TIA are needed. Thus, this results in the same aggregate bandwidth for a given number of electronic blocks. Furthermore, an AC-coupled receiver architecture can be used [33] and the TIA flicker-noise removed at low frequencies, provided a small frequency guard band ω_Δ is allocated by shifting down the frequency of the reference tone relative to the lower edge of the slice's passband. The smallest relevant detected beat-note frequency is then above ω_Δ, so that the frequency range around DC can be filtered out up to ω_Δ from the electronic signal path. It should be noted that in this architecture the balanced PD pair and differential TIA could also have been replaced by a single photodetector and a single-ended TIA in combination with digital post-processing using the Kramers-Kronig transform [34]. However, the fully differential architecture adopted here provides the maximal signal strength.

The part of the schematic framed by the green rectangle in Fig. 3(a) has been implemented in a silicon photonics ePIC that is currently under fabrication, with the corresponding layout shown in Fig. 3(b). Implementation of the spectrally-sliced ADC also involves the selection of a suitable MLL with low jitter, emission in the transparency window of silicon, and reasonable compactness. While Ti:sapphire lasers have shown the best jitter performance [7], their emission in the 650 to 1100 nm range prevents direct use with a silicon photonics ePIC. Erbium-doped fiber MLLs are an alternative with better compactness, higher robustness, and emission in the C-band. They can also reach the high repetition rates needed for the 30 GHz spectral slices implemented in our chip by means of internal filters without requiring an electric master oscillator [35,36]. In Fig. 4, the phase noise PSD of a best-in-class Er-fiber MLL [37] is compared to that of a record-low-jitter Ti:sapphire laser [7] as well as a state-of-the-art 10 GHz RF source based on an oven controlled quartz crystal oscillator (OCXO) [38]. The optical sources' spectra have been rescaled to a 10 GHz repetition rate. The timing jitter, as obtained from integrating the phase noise from 100 Hz to 10 MHz, is 6.4 fs for the electric oscillator, 870 attoseconds as for the Er-fiber MLL and only 1.75 attoseconds as for the Ti:sapphire laser (the phase noise below 300 Hz was extrapolated for the Er-doped fiber MLL following its almost ideal $1/f^2$ dependency). It is apparent that both MLLs offer significantly lower noise levels with respect to the OCXO, but while the Er-fiber MLL results in a timing jitter improvement by a factor ~7, the Ti:sapphire results in an improvement by over three orders of magnitude. To further improve performance, it might be possible to lock an Er-fiber MLL to a Ti:sapphire MLL to generate a reduced jitter pulse train at C-band wavelengths. Since the Er-fiber MLL features increased jitter relative to the Ti:sapphire mainly at low frequencies below 100 kHz, this might fall within the locking range of a phase locked loop, so that substantial phase noise reduction can be expected.

Optics EXPRESS

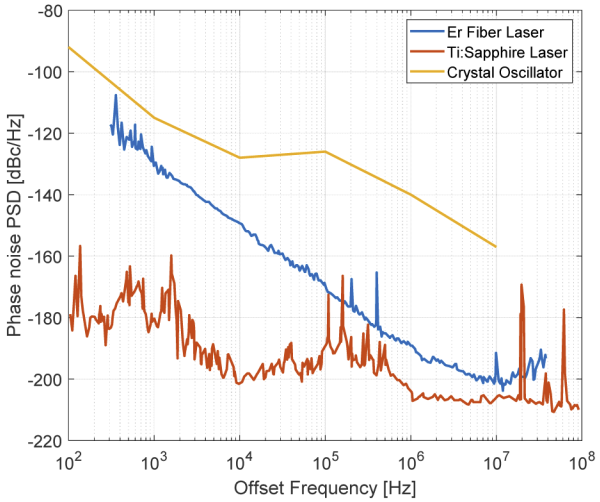

Fig. 4. SSB phase noise PSD of a low-jitter Er-fiber MLL [37] (blue), Ti:sapphire laser [7] (red) and quartz crystal oscillator [38] (yellow), all scaled to a 10 GHz oscillation frequency. Data digitized and replotted from [7,37].

3. System model

This section describes the assumptions made for the modeling of the single frequency laser and of the MLL (Subsection 3.1) as well as of the receiver slices (Subsection 3.2).

3.1. Mode-locked laser model

Following the derivation in [39], the MLL emission is described as a sum of N individual optical lines, whose real-time electric field is described as

$$E_{MLL}(t) = \left[\sum_{n=1}^{N} E_n e^{\mathrm{j}[\omega_n t+\theta_n(t)+\phi_n]}\right] + c.c. \tag{1}$$

where E_n, ω_n, $\theta_n(t)$ and ϕ_n are respectively the real-valued amplitude of individual comb lines indexed by n, their angular frequency, phase noise and static phase offset, as determined by dispersion inside the laser cavity [40] and inside the waveguides on the optical path between the laser and the PD pair. This model neglects amplitude noise, as the coefficients E_n are assumed to be constant. Phase noise usually dominates over amplitude noise, particularly at low noise frequencies [41]. Moreover, as will be discussed in more details in the following, the relative intensity noise (RIN) of the reference tones provided by the MLL can in principle be corrected if appropriate monitoring taps are implemented in the system. While the phase offsets ϕ_n need to be corrected by dispersion compensation in the optical domain in the time-interleaved architecture shown in Fig. 1(a), for the spectrally-sliced architecture analyzed in the following this dispersion compensation can also be implemented with digital signal processing after photodetection. This is further discussed in Subsection 3.2.

Assuming four-wave mixing (FWM), as mediated by a saturable absorber, or, in the case of single-section semiconductor lasers, by carrier density pulsation [42], to perfectly lock the phase of different comb lines, we obtain

$$\frac{d}{dt}[(2\omega_{n+1} - \omega_n - \omega_{n+2})t + (2\theta_{n+1}(t) - \theta_n(t) - \theta_{n+2}(t))] = 0 \tag{2}$$

Optics EXPRESS

leading, for any index n, to

$$\theta_{n+1}(t) - \theta_n(t) = \Delta\theta(t) \tag{3}$$

and

$$\omega_{n+1} - \omega_n = \omega_r \tag{4}$$

In these relations, ω_r is the beat-note frequency of the MLL, i.e., the pulse repetition rate or the free spectral range (FSR), and $\Delta\theta(t)$ is the phase noise observed in the beat note between two adjacent comb lines. Both $\Delta\theta(t)$ and ω_r are assumed to be independent of the pair of considered lines. We can then rewrite the MLL field as a function of the phase noise of the central line, $\theta_c(t)$, and the phase noise of the beat notes, $\Delta\theta(t)$, as

$$E_{MLL}(t) = \left[\sum_{n=1}^{N} E_n e^{\mathrm{j}[\omega_n t + \theta_c(t) + (n-n_c)\Delta\theta(t) + \phi_n]}\right] + c.c. \tag{5}$$

with n_c the index of the central comb line. Setting $\Delta\theta(t) = \omega_r \Delta t_r(t)$ and factoring out the phasor corresponding to the central line with angular frequency ω_c, we obtain

$$E_{MLL}(t) = e^{\mathrm{j}[\omega_c t + \theta_c(t)]}\left[\sum_{n=1}^{N} E_n e^{\mathrm{j}[(n-n_c)\omega_r(\Delta t_r(t)+t) + \phi_n]}\right] + c.c. \tag{6}$$

From this, $\Delta t_r(t)$ can be directly seen to be the timing jitter of the pulse train generated by the MLL. This expression is equivalent to assuming the MLL emission to be modeled by a carrier with angular frequency ω_c and optical phase noise $\theta_c(t)$ being modulated by a pulse train with angular repetition frequency ω_r and timing jitter $\Delta t_r(t)$, with associated RF phase noise $\Delta\theta(t)$, wherein the optical field undergoes additional dispersion as described by the phase offsets ϕ_n. Assuming perfect FWM as implied by Eq. (2) is thus equivalent to assuming that the shape of the pulses is conserved (after dispersion compensation), with the envelope function suffering only from timing-jitter. We now denote as $\Delta\omega_{r_m}$ the linewidth of the beat note between two optical lines spaced by $m\omega_r$, known also as the RF linewidth. This linewidth scales with the square of the phase noise $m\Delta\theta(t)$ [43], so that we obtain

$$\Delta\omega_{r_m} = m^2 \Delta\omega_{r_1} \tag{7}$$

expressing the quadratic dependence of the RF linewidth on the comb line spacing. Further assuming that the timing jitter $\Delta t_r(t)$ follows a Wiener process, since, due to spontaneous emission in the cavity, the phase noise follows a random walk, the spectrum of the RF beat notes is given by Lorentz functions whose full width at half maximum (FWHM) can be related to the walk-off of the pulse timing by [44]

$$\Delta t_r(t) = \frac{1}{\omega_r}\sqrt{\Delta\omega_{r_1} t} \tag{8}$$

In the numerical modeling described in Section 4, the optical phase noise of the single frequency laser, the optical phase noise of the central comb line and the RF phase noise of the pulse train are all assumed to follow Wiener processes. In the following, the subscript "1" is dropped in $\Delta\omega_{r_1}$ when it refers to the beat note between two adjacent lines.

3.2. Spectrally-sliced optically enabled ADC model

We now introduce the modeling assumptions made to describe the remainder of the system. As depicted in Fig. 3, an optical carrier is sent through a broadband electro-optic modulator,

Optics EXPRESS

transducing the electric signal that is to be digitized into an optical power. The field at the output of the modulator is described as its Fourier decomposition as

$$E_{MZM}(t) = e^{j\omega_0 t + j\theta_0(t)} \int_{\omega_s=-\omega_0}^{\omega_s=\infty} E_s(\omega_s) e^{j\omega_s t} d\omega_s + c.c. \tag{9}$$

where ω_0 and $\theta_0(t)$ are the angular frequency and the phase noise of the optical carrier sent through the modulator. ω_s is the frequency offset from the carrier and $E_s(\omega_s)$ is a complex amplitude that describes the time-dependent transfer function of the modulator, depending on the applied electric signal.

The electric field at the output of the modulator $E_{MZM}(t)$ is sliced into multiple spectral slices, each having a passband width ω_r matched to the FSR of the MLL. For the sake of simplicity, in this model the filter transfer functions used for slicing are assumed to be ideal square shaped without phase distortion. While in practice non-ideal filter transfer functions have to be addressed by digital post-processing, algorithms have been developed to achieve this [17] and it has no impact on the conclusions regarding fundamental jitter limitations drawn in the following.

At this point, a DCS combines each slice with a corresponding MLL comb line, with a center frequency offset ω_Δ below the lower edge of the slice to guard against electronic flicker noise, as explained in Section 2. The MLL reference tone is filtered with an OADM whose passband is also ω_Δ wide. As can be seen in Fig. 5, which illustrates the relative alignment of filters, MLL reference tones and optical carrier, this leaves a dead-zone of $\omega_\Delta/2$ between the highest reference tone frequency component and the lowest signal component in a given slice, ensuring that the signal can be reconstructed without the need of a 90-degree hybrid. While a dead-zone of zero would in principle have been sufficient based on this argument, this additional margin is required for subtler reasons explained in Section 4.

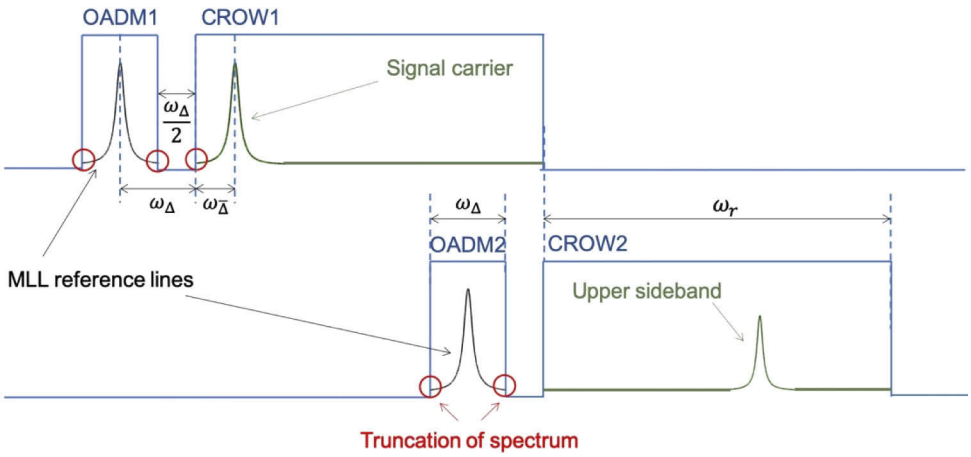

Fig. 5. Diagram of spectral alignment of the first two slices with MLL reference tones, signal carrier, and exemplary signal sideband. The CROW filters serving as passband filters to slice the signal are labeled as CROW1 and CROW2, the lower passband OADMs serving to singulate and route the MLL lines are labeled as OADM1 and OADM2. Red circles mark the truncation of reference tones and carrier spectra in the presence of phase noise (Lorentzian broadening).

Moreover, the spectral positions of the slices are configured to essentially only analyze the higher frequency sidebands of the optical signal. Ideally, this would correspond to the carrier of the incoming optical signal to be aligned with the lower edge of the lowest slice, so as to not waste any recording bandwidth. In practice, however, as will be discussed in Section 4, truncation of

Optics EXPRESS

the signal carrier in the presence of carrier phase noise reduces the overall SNR of the system. While this problem can be completely removed by analyzing the entire signal spectrum at the cost of doubling the required number of slices (see Section 4), here we alleviate it by pushing the signal carrier by an amount $\omega_{\overline{\Delta}}$ into the lowest slice to reduce the spectral truncation of the carrier. This comes at a very small cost in terms of overall bandwidth reduction.

The angular frequency of the MLL reference tone for the m^{th} slice, with index n_m, is then given by $\omega_{n_m} = \omega_0 - \omega_\Delta - \omega_{\overline{\Delta}} + m \cdot \omega_r$ and its field described by

$$E_{MLL,m}(t) = e^{\mathrm{j}(\omega_0 + m\cdot\omega_r - \omega_\Delta - \omega_{\overline{\Delta}})t + \mathrm{j}\theta_c(t)} E_{n_m} e^{\mathrm{j}[(n_m - n_c)\omega_r \Delta t_r(t) + \phi_{n_m}]} + c.c. \tag{10}$$

For a given slice, the field filtered from the modulator output is expressed as

$$E_{MZM,m}(t) = e^{\mathrm{j}(\omega_0 + m\cdot\omega_r)t + \mathrm{j}\theta_0(t)} \int_{\omega_s = m\cdot\omega_r - \omega_{\overline{\Delta}}}^{\omega_s = (m+1)\cdot\omega_r - \omega_{\overline{\Delta}}} E_s(\omega_s) e^{\mathrm{j}(\omega_s - m\cdot\omega_r)t} d\omega_s + c.c. \tag{11}$$

The combined signal is subsequently photo-detected by a pair of balanced PDs whose differential photocurrent is given by

$$i_m = \frac{1}{2}|E_{MZM,m}(t) + E_{MLL,m}(t)|^2 - \frac{1}{2}|E_{MZM,m}(t) - E_{MLL,m}(t)|^2 = \tag{12}$$

$$2e^{\mathrm{j}(\omega_\Delta + \omega_{\overline{\Delta}})t + \mathrm{j}(\theta_0(t) - \theta_c(t))} E^*_{n_m} e^{-\mathrm{j}[(n_m - n_c)\omega_r \Delta t_r(t) + \phi_{n_m}]} \cdot \int_{\omega_s = m\cdot\omega_r - \omega_{\overline{\Delta}}}^{\omega_s = (m+1)\cdot\omega_r - \omega_{\overline{\Delta}}} E_s(\omega_s) e^{\mathrm{j}(\omega_s - m\cdot\omega_r)t} d\omega_s + c.c.$$

The photocurrent i_m is digitized with a conventional electric ADC and sent on for digital data processing and aggregation, stitching together data from other slices. After digitization, the complex valued representation of the photocurrent i_m is computed by calculating its harmonic conjugate with the Hilbert transform $H(i_m)$ and adding them in quadrature. The corresponding complex valued phasor can be reconstituted with the Hilbert transform, as all the signal frequencies lie above the reference tone components and the beat notes can thus be unambiguously mapped to positive frequencies. The resulting complex phasor is then digitally shifted in frequency by $m\omega_r$ and added to the data from other slices, at which point the E-field at the output of the modulator $E_{MZM}(t)$ is recovered. The result is then squared to recover the analyzed signal, since it is carried by the optical power at the output of the modulator. The power of each comb line $P_{n_m} = |E_{n_m}|^2$ is assumed to be known, since it can be straightforwardly measured with an optical tap implemented after the corresponding OADM. The static phase offset ϕ_{n_m} is also assumed to be measured and to be corrected for. It can be simply obtained by measuring sinusoidal RF pilot tones generating sidebands at predetermined frequency offsets, or by analyzing data in the frequency range of partially overlapping slices [17]. By comparing the phase of a reconstructed sine tone to that of the initial pilot tone sent to the electro-optic modulator, the static phase error at the corresponding frequency offset can for example be directly determined, as it is equal to the phase delay between the input and output signals, and subsequently digitally compensated by a one tap equalization. The reconstructed signal is thus given by

$$S = \left| \sum_m \frac{(i_m + \mathrm{j}\cdot H(i_m))}{\sqrt{P_{n_m}}} e^{\mathrm{j}m\omega_r t + \mathrm{j}\phi_{n_m}} \right|^2 = \tag{13}$$

$$16 \left| \sum_m e^{-\mathrm{j}m\omega_r \Delta t_r(t)} \int_{\omega_s = m\cdot\omega_r - \omega_{\overline{\Delta}}}^{\omega_s = (m+1)\cdot\omega_r - \omega_{\overline{\Delta}}} E_s(\omega_s) e^{\mathrm{j}\omega_s t} d\omega_s \right|^2$$

It is clear that in the case of an ideal MLL with no pulse train jitter, i.e., with $\Delta t_r(t) = 0$, the optical power at the output of the modulator can be perfectly reconstructed. In the realistic case

Optics EXPRESS

where, instead, the MLL is affected by a non-zero timing jitter $\Delta t_r(t)$, the performance of the ADC degrades, as will be discussed in more details in the next section.

It should be noted here that the truncation of the MLL reference tones by the OADMs has not been taken into account in the derivation of Eq. (13). As this can also contribute, albeit to a lesser extent, to system-level noise, it will also be analyzed in the following.

4. Analytical SNR model and numerical verification

This section is dedicated to the description of numerical modeling results, as well as to the derivation and validation of compact analytical formulas predicting the SNR of the optically enabled spectrally-sliced ADC. Subsection 4.1 describes assumptions made in regards to laser characteristics, as also constrained by the code's memory requirements due to the multi-scale nature of the simulated problem. Subsection 4.2 describes the actual numerical results and analytical formulas. In Subsection 4.3, we discuss the practicability of implementing phase noise trackers in the digital domain and show that this is not conducive to improving jitter performance unless another, better reference clock is provided.

4.1. Assumptions and implementation specific limitations

Assumptions made in regards to laser characteristics as well as time steps and time interval of the implemented simulation code are summarized in Table 1.

Table 1. Model assumptions (optical noise, system characteristics and simulation settings). Linewidths and guard bands are given as ordinary frequencies referred to with the letter *f*.

Parameter	Symbol	Value	Unit
Optical linewidth of carrier (3 dB)		100	kHz
Optical linewidth of central MLL line (3 dB)		10	MHz
RF linewidth of MLL (3 dB)	Δf_r	3	kHz
Gaussian pulse width ($1/e^2$)		1.6	ps
FSR of MLL / slice width	f_r	30	GHz
OADM passband (MLL line filtering)		2	GHz
Offset f_Δ	f_Δ	2	GHz
Offset $f_{\overline{\Delta}}$	$f_{\overline{\Delta}}$	2	GHz
Electric ADC sampling rate		75	GBd
Electric ADC analog bandwidth		> 32	GHz
Time step		0.3	ps
Time interval	t_{sim}	3.3	µs

Non-idealities considered in this model are the optical phase noise of the carrier and of the central MLL line (the correlated part of the phase noise), both modeled as Wiener processes and expressed as optical linewidths. The timing jitter of the MLL pulse train and of the electric oscillator used to supply clocks to the electric ADCs inside the individual slices are also taken into account. Pulse / electric clock timing are also described by Wiener processes and expressed in terms of RF / electrical linewidths. The FSR of the MLL is set to 30 GHz to correspond to the target of the hardware we are developing. Since we are simulating 4 slices analyzing an RF signal up to an aggregate bandwidth of 120 GHz, this constrains the time-step in the code to be below 4 ps to prevent aliasing. Here we set it to slightly below $1/10^{\text{th}}$ of this value, i.e., to 0.3 ps.

As seen in Table 1, we set the RF linewidth of the MLL to 3 kHz, corresponding to a timing jitter of 16.4 ps in the 100 Hz to 10 MHz range. This was the minimum value we could simulate, constrained by memory limitations and the requirement that the simulation time t_{sim} needs to

Optics EXPRESS

be long enough to incur significant phase noise. The phase noise associated to the MLL RF linewidth $\Delta\omega_r$, expressed as an angular frequency, has a std. dev. $\sqrt{\Delta\omega_r t_{sim}}$ [43] at the end of the simulation. Given the 3.3 µs simulation time and the 3 kHz linewidth, this std. dev. is 0.25 rad and already quite small. Thus, simulating the system with a 3 kHz linewidth already requires in the order of 10 million time-steps with the followed method. The optical linewidth of an MLL is typically orders of magnitude larger than its RF linewidth, so that we assume here 10 MHz for the optical linewidth of the central MLL line. The optical carrier sent through the electro-optic modulator is assumed to be generated by an external cavity laser (ECL) and its linewidth is set to a typical value of 100 kHz.

Incidentally, the numbers assumed for the MLL are in the bulk part of what can be straightforwardly obtained with a state-of-the-art solitary semiconductor MLL [40]. The RF linewidth and the associated pulse train timing jitter are, however, much worse than those of a conventional OCXO and numerical results by themselves are not representative of what can be accomplished with low jitter MLLs [7,9,37]. Their noise levels are so low that their direct modeling is entirely out of reach of the code utilized here. However, as the noise sources are analyzed one-by-one in the following, exaggerated noise levels do not preclude drawing the right conclusions, as resulting system level noise can be rescaled. Rather, analytical models are validated with the code and can be used to extrapolate the performance of the system for different types of realistic MLLs. This is discussed in Section 6.

Due to the guard band f_Δ, the required electronic bandwidth in the receiver slices is increased from 30 GHz to 32 GHz and the minimum electronic ADC sampling rate is increased from 60 GBd to 64 GBd. While the requirement for f_Δ scales with the optical linewidth of the MLL and could in principle be reduced with a better laser, it would also result in a requirement for a narrower OADM passband. Since passbands below 2 GHz could prove challenging to realize on chip with standard silicon technology, we have not further considered this here.

Electric ADCs are modeled in the following as a sampling operation triggered by an electric clock, allowing the modeling of electric ADC jitter in the next subsection, in which a general jitter model is derived. Digitization, i.e., the quantization noise of the electric ADCs, is not modeled, as it does not fall inside the scope of the fundamental jitter limitations analyzed here and would interfere with drawing general conclusions in regards to the latter.

4.2. System performance analysis

We report simulation results for system performance in presence of (i) phase noise from the optical carrier sent through the electro-optic modulator, (ii) phase noise from the central MLL comb line, and (iii) RF phase noise from the pulse train generated by the MLL. We then move on to also include electric oscillator noise and derive a comprehensive performance model.

Starting with (i), we show the example of a sinusoidal RF signal with a frequency of 100 GHz, i.e., with a sideband falling inside the 4^{th} slice of the system, being processed in presence of carrier phase noise only. All other sources of noise, including those arising from the MLL and from electronic digitization, are turned off in this simulation. In Fig. 6(a), the optical power at the output of the modulator, labeled as "Signal In" on the x-axis, is compared to the reconstructed signal obtained after detection and signal post-processing. Two non-idealities are apparent in the form of signal distortion and noise.

The conversion of carrier phase noise into noise at the output of the ADC was unsuspected based on Eq. (13). In fact, this system level noise is unrelated to signal reconstruction and is related to the distortion also seen in Fig. 6(a). Both are due to the fact that the four slices used to record the signal have a finite overall bandwidth of 120 GHz and are thus truncating the signal spectrum (Fig. 7). In particular, the sidebands with frequencies below the carrier are truncated, resulting in the observed signal distortion. Since these are the complex conjugates of the upper frequency sidebands, they could be straightforwardly reconstructed from the latter with

Optics EXPRESS

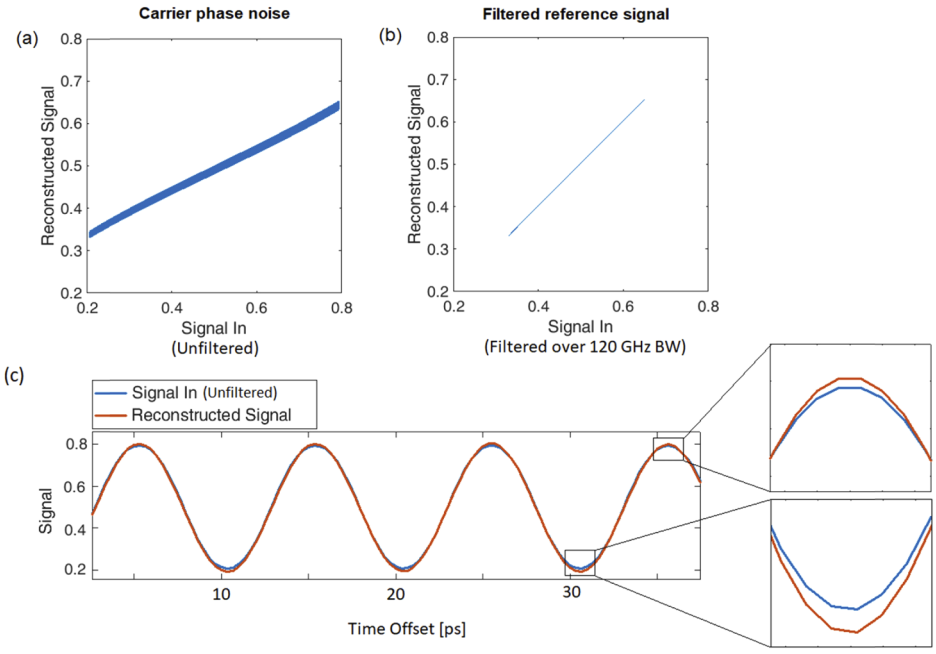

Fig. 6. (a) Reconstructed 100 GHz signal, after digitization employing 4 slices (120 GHz overall bandwidth), plotted against the signal at the output of the modulator. Carrier phase noise is turned on, but optical and RF MLL phase noise, as well as electric oscillator phase noise are turned off. Some amount of distortion and system level noise are apparent. In (b) the reconstructed signal is plotted against the power of the optical signal at the output of the modulator after filtering by an equivalent ideal 120 GHz passband filter. The perfect correlation of both signals confirms the finite bandwidth of the system to be the root cause of both distortion and noise. In (c) the evolution in time of the unfiltered input signal as well as of the reconstructed signal are plotted. The noise takes the form of a time varying deviation of the reconstructed signal amplitude with respect to the input reference signal. The amplitude of the reconstructed signal has been doubled in this graph to compensate for only one sideband being recorded.

digital signal processing and the distortion corrected. This is verified in Fig. 6(b) in which the reconstructed signal is plotted against the input signal after filtering by an equivalent 120 GHz passband. The reconstruction is perfect relative to this reference, pointing to the noise seen in Fig. 6(a) also being caused by the truncation.

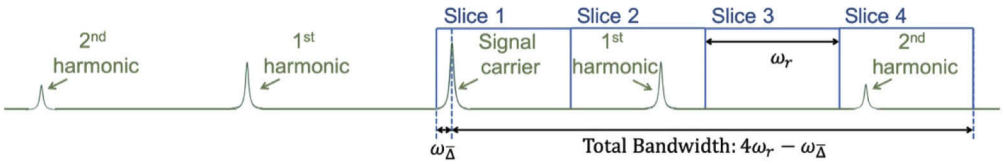

Fig. 7. Truncation of the signal bandwidth after recording with four spectral slices. Here, an exemplary signal has a 1st harmonic in the 2nd slice and a 2nd harmonic in the 4th slice. Higher order harmonics and side-bands below the carrier are filtered out. The carrier is pushed $\omega_{\overline{\Delta}}$ into the 1st slice, the overall system bandwidth is $4\omega_r - \omega_{\overline{\Delta}}$.

Optics EXPRESS

In the presence of optical carrier phase noise, the tail of the Lorentzian distribution of the carrier PSD is being truncated at the lower edge of the lowest slice. Since the spectral broadening of the carrier is due to phase noise, the information to rebuild these frequency components is lost in the general case, as it cannot be distinguished from in-band, low speed input signal components. Thus, carrier phase noise matters to some extent in that it constrains the guard band $f_{\overline{\Delta}}$ required for low system-level noise operation (Fig. 7). In Fig. 6(a), a guard band of 2 GHz was chosen (2×10^4 times the 100 kHz ECL linewidth), that represents a modest penalty compared to the remaining 118 GHz system bandwidth. Pushing the carrier deeper into the lowest slice would result in further reduction of carrier truncation and consequently of this noise.

We proceed by analyzing the effect of MLL non-idealities on the reconstructed signal, first only turning on the phase noise of the underlying carrier (i.e., the phase noise of the central line), further assuming the RF phase noise of the MLL and the optical phase noise of the carrier sent through the modulator to be zero [scenario (ii)]. A sinusoidal RF signal with a frequency of 100 GHz has been processed once more through the system, with the MLL comb lines having an optical linewidth of 10 MHz with perfectly correlated phase noise.

Results are shown in Fig. 8(a). Again, we observe some system level noise not directly predicted by Eq. (13). The noise in the reconstructed signal appears to be proportional to the input signal strength and cannot be modeled as jitter. Rather, we were able to track it down as being caused by RIN in the reference tones generated by the MLL. While we assumed the absolute amplitudes E_n of the comb lines to be constant over time, this does not remain true after optical filtering via the OADMs. As explained in Section 3, the reference tone needs to be clipped towards positive frequencies to prevent reference tone frequency components to be above the lowest signal frequency in a given slice. This clipping, even if implemented symmetrically on both sides at $\pm\omega_\Delta/2$ away from the central carrier frequency (as shown in Fig. 5), converts some of the phase noise into amplitude noise, so that after the OADM the assumption of E_n being a constant no longer holds true.

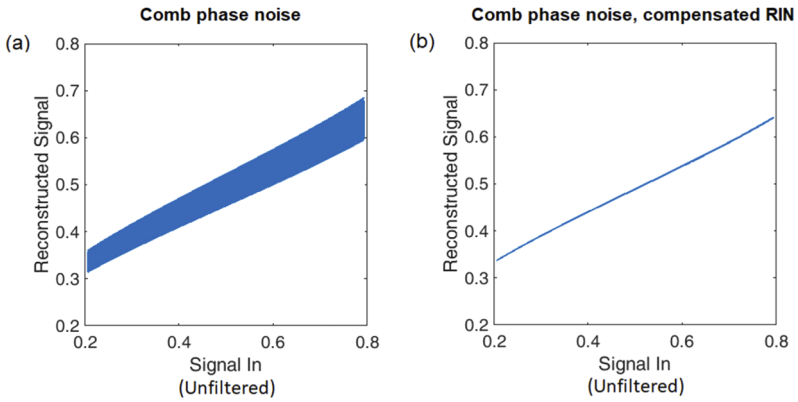

Fig. 8. (a) Reconstructed 100 GHz signal, after digitization employing 4 slices (120 GHz overall bandwidth), plotted against the signal at the output of the modulator. The correlated optical phase noise of the comb is turned on, but all other noise sources are off. RIN generated by spectral truncation of the reference tones is reflected in the system level performance in the form of signal strength dependent noise. After normalizing out the reference tone RIN, noiseless signal reconstruction is recovered (b).

We re-simulated the system assuming a tap right after the OADM to measure the instantaneous optical power $P_n(t)$, so that it can be taken into account in Eq. (13) by replacing the normalization with the constant (average) line power level by a normalization with the instantaneous line power.

Optics EXPRESS

Results are shown in Fig. 8(b). It is apparent that this fully accounts for the observed system noise and that near-noiseless signal reconstruction is again achieved.

This is also the reason why we needed a dead-zone of width $\omega_\Delta/2$ between the passbands of the OADM and of the slice. Measuring the power $P_n(t)=|E(t)|^2$ and subsequently dividing by $1/\sqrt{P_n(t)}$ consists in a series of non-linear operations that effectively broaden the spectrum of the filtered MLL reference tone (the operation, done after detection in the digital domain, is equivalent to a direct transformation of the reference tone spectrum). After the operation, most of the power remains in an interval $\pm\omega_\Delta$ around the reference tone center frequency, so that the width of the guard band proved to be sufficient (see Fig. 5 for spectral alignments).

We now assess the effect of MLL pulse jitter, as described by the RF linewidth under the assumption of the RF phase noise being subjected to a Wiener process. All other sources of noise, including the optical phase noise of the central MLL line, are turned off [scenario (iii)].

From Eq. (13), it can be seen that if the entire optical spectrum fits into one slice, the RF phase noise of the MLL is irrelevant, as the phasor $e^{-jm\omega_r\Delta t_r(t)}$ can then be factored out from the summation and is subsequently voided when the absolute value is taken. In this instance, the performance of the optically enabled ADC is only limited by the jitter of the electric oscillator supplying the clock of the electric ADCs used in the individual slices, as will be analyzed in detail below. On the other hand, if the optical signal contains E-field components in several slices, the MLL timing jitter plays an important role.

Once again, a sinusoidal RF signal with a frequency of 100 GHz, corresponding to a sideband in the 4$^{\text{th}}$ slice, has been exemplarily processed considering an MLL RF linewidth of 3 kHz. As can be seen from the results shown in Fig. 9(a), the reconstructed signal is now significantly deteriorated by the RF phase noise of the MLL, even though the 3 kHz linewidth is much smaller than the optical linewidths considered above. The system level noise is, as expected in the case of timing jitter, more pronounced at the mid-signal-level, where the sinusoidal input signal has its highest slope. The finite RF linewidth can thus be seen to result in sampling time jitter. The histogram of the reconstructed signal error, taken over sampling times where the input signal is mid-level and has maximum slope, is plotted in Fig. 9(b). As simulation times increase, the sampled signal further deteriorates as expected in case of jitter, presenting a different behavior compared to the previously investigated noise sources that maintain a bounded std. dev. irrespectively of the simulation time.

The impact of timing jitter coming from the MLL can be derived and generalized starting from Eq. (13). Assuming the optical field at the output of the modulator to contain frequency components between $m\omega_r$ and $(m+1)\omega_r$, falling into the m^{th} slice, with m larger than 0, in addition to the carrier falling into the lowest slice with index 0, the E-field will contain components in at least two slices spaced by $m\omega_r$, whose beat note will generate the time-varying reconstructed signal after summation and squaring. Denoting the carrier and the corresponding signal sideband as $E_s(\omega_{s,0})=E_{s,0}\delta(\omega=\omega_{s,0})$ and $E_s(\omega_{s,m})=E_{s,m}\delta(\omega=\omega_{s,m})$, the corresponding slice indices as n_0 and n_m, and the angular frequency of the digitized RF tone as $\omega_{RF}=\omega_{s,m}-\omega_{s,0}$, Eq. (13) reduces to

$$S = 16|e^{-\mathrm{j}n_0\omega_r\Delta t_r(t)}E_{s,0}e^{\mathrm{j}\omega_{s,0}t} + e^{-\mathrm{j}n_m\omega_r\Delta t_r(t)}E_{s,m}e^{\mathrm{j}\omega_{s,m}t}|^2 = \tag{14}$$
$$16(|E_{s,0}|^2 + |E_{s,m}|^2 + 2Re(E^*_{s,0}E_{s,m}e^{\mathrm{j}\omega_{RF}t-\mathrm{j}m\omega_r\Delta t_r(t)}))$$

If m is large, i.e., the RF signal frequency ω_{RF} is large compared to the bandwidth ω_r of a single slice, the approximation $m\omega_r \approx \omega_{RF}$ can be made and the recovered sinusoidal function takes the simplified form

$$S \simeq 16(|E_{s,0}|^2 + |E_{s,m}|^2 + 2Re(E^*_{s,0}E_{s,m}e^{\mathrm{j}\omega_{RF}(t-\Delta t_r(t))})) \tag{15}$$

The jitter of the MLL pulse train, $\Delta t_r(t)$, is then directly applied to the sampling performed by the optically enabled ADC. In the general case, however, the applied jitter is rescaled as $(m\omega_r/\omega_{RF})\Delta t_r(t)$, i.e., the RF signal frequency is rounded down to the next lower integer number

Optics EXPRESS

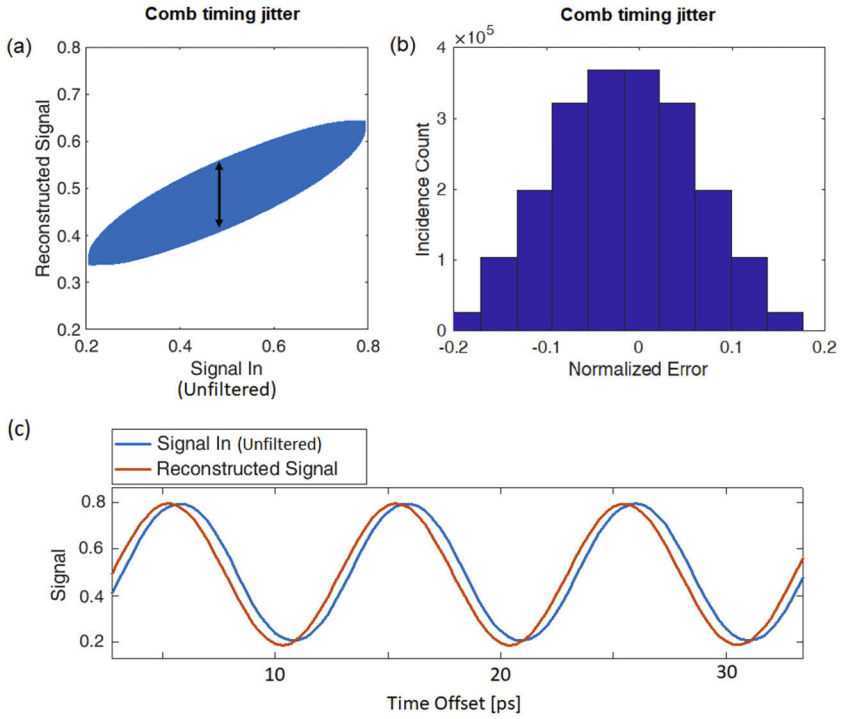

Fig. 9. (a) Reconstructed signal, after digitization employing 4 slices (120 GHz overall bandwidth), plotted against the signal at the output of the modulator. The pulse train of the MLL is assumed to be subjected to timing jitter corresponding to a 3 kHz linewidth, all other sources of noise are turned off. We observe noise levels in the recovered signal that are proportional to the derivative of the input signal. The histogram of the error at the sampling points corresponding to a mid-level input signal (black arrow in (a)) is shown in (b). In (c), the time evolution of the unfiltered input signal and of the reconstructed signal are plotted. The noise can be seen to take the form of a time offset between the reconstructed signal and the input reference signal that slowly varies as further RF phase noise is being accumulated, representing the sampling uncertainty. As in Fig. 6, the reconstructed signal is doubled to compensate for the fact that only one of the two sidebands is being recorded.

of slices. In general, the SNR of an ADC with aperture jitter Δt and angular signal frequency ω is limited by [1]

$$\mathrm{SNR} = 20log_{10}\left[\frac{1}{\omega \cdot \Delta t}\right] \tag{16}$$

Plugging in the rescaled MLL jitter, we obtain

$$\mathrm{SNR} = 20log_{10}\left[\frac{1}{m\omega_r \cdot \Delta t_r(t)}\right] \tag{17}$$

expressing the limitation of the SNR of our spectrally-sliced ADC due to the MLL jitter.

Of course, the timing jitter of the electric oscillator driving the ADCs in the individual slices also plays an important role in the signal recovery. We denote the jitter of the electric clock as $\Delta t_e(t)$ and, further assuming it to be subjected to a Wiener process, we associate the jitter to the Lorentzian linewidth of the electric oscillator used to generate it according to

$$\Delta t_e(t) = \frac{1}{\omega_e}\sqrt{\Delta\omega_e t} \tag{18}$$

Optics EXPRESS

where ω_e is the angular frequency of the electric oscillator and $\Delta\omega_e$ its linewidth. The Lorentzian linewidth assumption is not fundamental for the derivations, that can also be done directly in terms of timing-jitter $\Delta t_e(t)$, but a conversion into a linewidth $\Delta\omega_e$ helps the discussion in the following, as it is the main metric with which optical oscillators have been specified.

In a fully electric ADC, the effect of oscillator jitter would be frequency dependent as expressed by Eq. (16) – also showing the direct tradeoff between signal bandwidth and ENOB given a certain aperture jitter – and as depicted by the yellow curve in Fig. 10. In our system, however, the overall signal frequency has to be replaced by the down-converted frequency seen by the electric ADC in a given slice, $\delta\omega_m = \omega_{RF} - m\omega_r + \omega_\Delta + \omega_{\overline{\Delta}}$. This down-converted frequency lies between ω_Δ and $\omega_r + \omega_\Delta \approx \omega_r$, and is thus typically much lower than the actual input signal frequency, resulting in a substantial reduction of electric aperture-jitter noise.

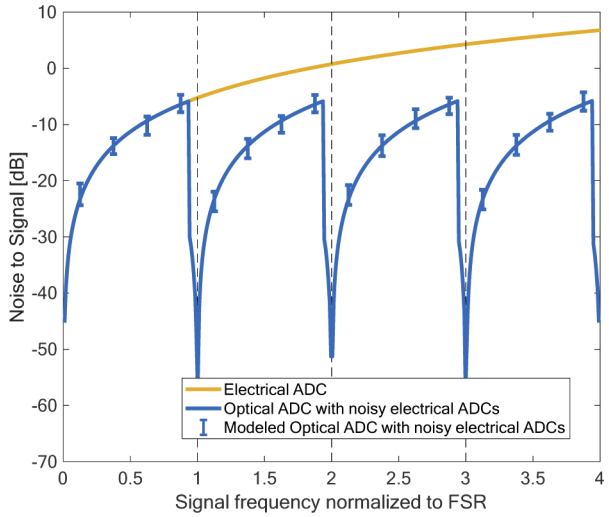

Fig. 10. Noise-to-signal ratio of a fully electric ADC (yellow) and of a spectrally-sliced ADC with four slices and as many parallel electric ADCs (blue), assuming electric oscillator phase noise to be the only noise source. Analytically modeled curves are shown by solid lines. Results from simulations are plotted with their 3σ confidence intervals shown by vertical bars.

Electrical aperture-jitter related noise is generated by ADCs digitizing both the optical carrier as well as the optical sideband. Since both ADCs are supplied by the same clock, their jitter is assumed to be correlated. The reconstructed signal can then be expressed as

$$S = 16|e^{j\delta\omega_0(t-\Delta t_e(t))} + e^{j\delta\omega_m(t-\Delta t_e(t))}e^{jm\omega_r t}|^2 \tag{19}$$

wherein the electric signal from slice m has been upconverted by digital signal processing, as previously explained. The time varying portion of S is then given by

$$S = 32 \cdot \cos((\delta\omega_m + m\omega_r - \delta\omega_0)t - (\delta\omega_m - \delta\omega_0)\Delta t_e(t)) = \tag{20}$$

$$32 \cdot \cos(\omega_{RF}t - (\omega_{RF} - m\omega_r)\Delta t_e(t))$$

It is thus apparent that the total electric-jitter aperture noise can be evaluated based on the residual of the input signal frequency ω_{RF} once $m\omega_r$ has been subtracted, with m the index of the slice in which the sideband falls, irrespectively of the guard bands ω_Δ and $\omega_{\overline{\Delta}}$. This is a consequence of the phase noise correlation. In case of uncorrelated electric oscillator phase noise, the term $(\delta\omega_m - \delta\omega_0)\Delta t_e(t)$ in Eq. (20) would need to take the two independent random processes into

Optics EXPRESS

account and would consequently have a std. dev. given by $\sqrt{\delta\omega_m^2 + \delta\omega_0^2}\sqrt{\langle \Delta t_e(t)^2 \rangle}$ instead of $|\delta\omega_m - \delta\omega_0|\sqrt{\langle \Delta t_e(t)^2 \rangle}$. The model described by Eq. (20) has been verified numerically:

In the following simulations, the linewidth of the electric oscillator has been assumed to be 180 kHz in order to ensure that it is significantly larger than the RF linewidth of the MLL. Assuming a realistic electric oscillator linewidth, in the order of 560 μHz for an OCXO upconverted to the 75 GHz electrical clock rate, would result in the corresponding phase noise to be negligible relative to the assumed MLL phase noise (assuming a Wiener process, the linewidth Δf in ordinary frequencies scales as $\Delta f = \pi f^2 S_\theta(f)$, with f the signal frequency and $S_\theta(f)$ the single-sided phase noise PSD [43,44]). As explained above, the assumed 3 kHz MLL RF linewidth was chosen mainly due to numerical simulation constraints. Best-in-class Ti:sapphire MLLs have been shown to yield a phase noise PSD about 3 orders of magnitude better than that of best-in-class electric sapphire crystal oscillators and reported Er-doped fiber lasers [37] outperform conventional OCXO by almost two orders of magnitude. Assuming the electrical linewidth to be two orders of magnitude worse than the MLL linewidth is thus equivalent to practically relevant scenarios. In other words, we assume the electric oscillator noise to be scaled up by the same amount as the MLL RF phase noise, in order to verify its interaction with the other dominant source of jitter.

The inverse of the corresponding SNR, in the absence of MLL noise, is plotted by the blue curve in Fig. 10. The theoretical curve corresponding to the model described above (solid blue line) is overlaid by results from the numerical model, with error bars showing the 3σ confidence interval of the SNR estimates obtained by running 65 simulations for each data point. Here and in Fig. 11 below, theoretical curves were obtained by modeling $\omega_{e,r}\sqrt{\langle \Delta t_{e,r}(t)^2 \rangle}$ as $\sqrt{\Delta\omega_{e,r} t_{sim}/2}$, i.e., taking into account that squared phase errors were averaged over the entire duration of the simulations resulting in an effective time of $\sqrt{\langle t^2 \rangle} = t_{sim}/2$.

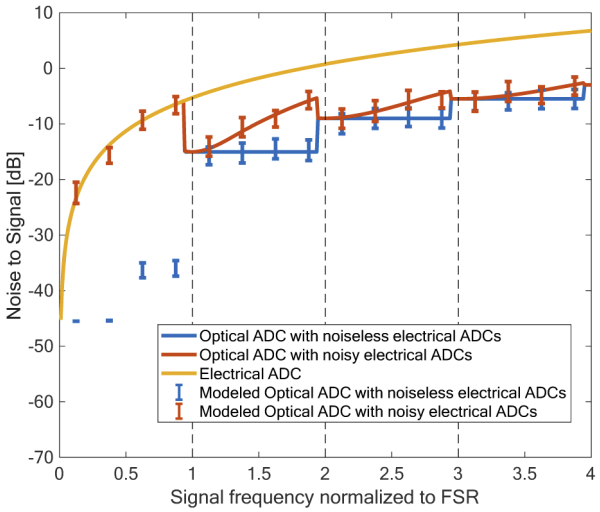

Fig. 11. Noise-to-signal ratio of the optically enabled ADC as a function of the RF input signal frequency. Solid lines correspond to Eq. (21) in the presence of electric oscillator phase noise only (yellow, for an all-electric ADC), MLL jitter only (blue), or a combination of both (red). Theoretical estimates are overlaid by simulation results with error bars showing the 3σ confidence intervals.

It is apparent in Fig. 10 that the numerical simulations coincide very well with the analytical model described above. There are two interesting features that can be seen in the curve. For one, the noise drops abruptly whenever the optical sidebands move to the next higher slice, as the

Optics EXPRESS

residue $\omega_{RF} - m\omega_r$ then abruptly drops by ω_r. These transitions occur slightly before the signal frequency ω_{RF} reaches an integer value of slice widths due to the small guard band $\omega_{\overline{\Delta}}$. The second feature is that the electric aperture jitter induced noise drops to zero for signal frequencies exactly equal to an integer number of slice widths. At these frequencies, the frequency offsets $\delta\omega_0$ and $\delta\omega_m$ are exactly equal to each other, so that the noise predicted by Eq. (20) is zero. Generalizing Eq. (17) to take into account both MLL and electric oscillator phase noise, we obtain the formula

$$\mathrm{SNR} = 20log_{10}\left[\frac{1}{\sqrt{[m\omega_r \cdot \Delta t_r(t)]^2 + [(\omega_{RF} - m\omega_r) \cdot \Delta t_e(t)]^2}}\right] \tag{21}$$

Errors induced by MLL and electric oscillator jitter are added as sum of variances as the two random processes are uncorrelated. Thus, the phase noise performance is limited by the MLL jitter in association with $m\omega_r$, essentially rounding down the signal frequency to the next lower integer number of slices. The remaining signal frequency $\omega_{RF} - m\omega_r$ enters the equation in combination with the electric oscillator jitter. It can be seen from Eq. (21) that the optically enabled ADC results in a net reduction of aperture jitter provided $\Delta t_r(t) < \Delta t_e(t)$, even though electric oscillator jitter still plays a role.

The inverse of the theoretical SNR expressed by Eq. (21) is plotted as a function of signal frequency in Fig. 11 for different scenarios, taking into account respectively electric oscillator jitter only in an all-electric ADC, MLL jitter only, and the combination of the two (solid yellow, blue and red lines). Here too, the theoretical SNR is overlaid by numerical results from the stochastic simulations, with error bars again indicating the 3σ confidence intervals. For each signal frequency 65 simulations were run. These validate the analytical model.

4.3. Phase noise compensation techniques

In the following, the possibility of implementing phase tracking algorithms in the DSP is briefly discussed. In principle, the beat note between two neighboring comb lines could for example be monitored to extract the RF phase noise $\Delta\theta(t)$ so that it could be compensated during post processing in addition to ϕ_n (as discussed in Section 3.2). However, during measurement of the beat note, the phase noise of the electric oscillator would also be picked up. In the attempt of canceling the term $e^{-\mathrm{j}(n_m - n_0)\omega_r \Delta t_r(t)}$ occurring in the photocurrent of the m^{th} slice [Eq. (12)], the phase noise recorded from the beat note between two adjacent comb lines, $\omega_r \Delta t_r(t)$, would have to be up-converted by a factor $n_m - n_0 = m$. This results in the PSD of the incurred electric oscillator phase noise to increase by a factor m^2 [1]. Similarly, up-converting the electric oscillator with a phase locked loop (PLL) in order to provide a reference tone to directly measure a higher order beat note between non-neighboring comb lines would result in the electric phase noise to scale up by the same factor. Thus, the MLL phase noise term $m\omega_r \Delta t_r(t)$ in Eq. (21) would simply be replaced by $m\omega_r \Delta t_e(t)$, which is counterproductive when the electric oscillator jitter $\Delta t_e(t)$ is larger than the timing-jitter $\Delta t_r(t)$ of the pulse train generated by the MLL. Tellingly, Eq. (21) would be rewritten as

$$\mathrm{SNR} = 20log_{10}\left[\frac{1}{m\omega_r \cdot \Delta t_e(t) + (\omega_{RF} - m\omega_r) \cdot \Delta t_e(t)}\right] = \tag{22}$$

$$20log_{10}\left[\frac{1}{\omega_{RF} \cdot \Delta t_e(t)}\right]$$

showing that the performance of the ADC would simply revert to that of a fully electric ADC, nullifying the aperture-jitter improvements of the optically enabled architecture. The sum of variances has been replaced by a direct sum as the two phase noise terms are now correlated.

Optics EXPRESS

On the other hand, locking the electric oscillator to the MLL in order to remove electric oscillator jitter would be conducive when the MLL is the lowest jitter oscillator in the system [45]. In this case, the SNR of the ADC would be limited by the MLL jitter only [i.e., replace $\Delta t_e(t)$ by $\Delta t_r(t)$ in Eq. (21), as well as the sum of squares and square root by a simple sum, again because of phase noise correlation]. This would lead to a net improvement of the overall system performance.

5. Noise limitations in spectrally-sliced DACs

Equation (21), that has been derived for an optically enabled spectrally-sliced ADC, can be straightforwardly generalized to the spectrally-sliced DAC architecture shown in Fig. 2. As the derivation is very similar to that of the spectrally-sliced ADC, we will proceed through it faster here – the reader may refer to Sections 3 and 4 for more details.

In this system, the MLL is the only optical source, with the optical phase noise of the central comb line and the RF phase noise the two dominant sources of optical noise. Since the optical power detected by the photodetector results from the beat notes between optical signal components, the correlated phase noise affecting MLL lines cancels out, as for the ADC. Similarly, narrow filtering of the comb lines would lead to some amount of RIN, even though here the only constraint on the filter bandwidth is the FSR of the laser, so that the comb line selection filters can be chosen to be very wide and this should not be a problem. Single sideband modulation is assumed to be obtained with an IQ modulator with the nested Mach-Zehnder modulators biased at their zero transmission point, so that additional filtering of the modulated carrier is not required. The uncorrelated optical phase noise, corresponding to the RF phase noise $\Delta\theta(t)$, however remains, as previously, and grows as $(n_m - n_0)\,\Delta\theta(t) = m\Delta\theta(t)$ as the spacing between the relevant comb lines increases.

To convert an RF signal at a frequency ω_{RF} falling in the range $[m\omega_r, (m+1)\omega_r]$, an optical carrier needs to be generated in the slice of index 0, the lowest or central slice in case of dual sideband generation. An optical sideband needs to be generated in the slice of index m. These are generated with single-sideband modulators from MLL lines n_0 and n_m. Consequently, the beat note generated by optically combining and photo-detecting the two slices will carry a phase noise $m\Delta\theta(t)$. The corresponding timing jitter can be expressed as

$$\Delta t(t) = \frac{1}{\omega_{RF}}\sqrt{\Delta\omega_{r_m} t} \tag{23}$$

Plugging Eq. (7) into Eq. (23) we obtain

$$\Delta t(t) = \frac{1}{\omega_{RF}}\sqrt{m^2\Delta\omega_{r_1} t} = \frac{m\omega_r}{\omega_{RF}}\Delta t_r(t) \tag{24}$$

corresponding exactly to the system level timing jitter already derived as Eq. (17) for the spectrally-sliced ADC. As for the ADC, the other non-ideality to be taken into account is the timing jitter introduced by the fully electric data converters used in each slice.

Once again, we model the electric oscillator phase noise as a Wiener process, expressing the timing jitter as a function of the Lorentzian linewidth of the oscillator used to generate the DAC triggers, according to Eq. (18). We obtain an SNR given by

$$\mathrm{SNR} = 20log_{10}\left[\frac{1}{\sqrt{[m\omega_r \cdot \Delta t_r(t)]^2 + [(\omega_{RF} - m\omega_r)\cdot \Delta t_e(t)]^2}}\right] \tag{25}$$

equivalent to what was obtained for the optically enabled ADC.

Optics EXPRESS

The numerical model of the spectrally-sliced ADC is adapted to also model the spectrally-sliced DAC, with the same assumptions made in regards to slice width, number of slices, RF and optical linewidths, and sample rates / analog bandwidth for the electric data converters (Table 1).

In Fig. 12, the analytical model given by Eq. (25) (solid lines) is compared to the numerical model, respectively for a fully electric DAC with electric oscillator phase noise (yellow), an optically enabled DAC without electric oscillator noise but with MLL RF phase noise (blue), as well as an optically enabled DAC with both electrical and optical phase noise (red). As previously, numerical estimates are obtained with 65 simulations with 3σ confidence intervals shown by error bars. Here too, the analytical model is validated by the numerical simulations.

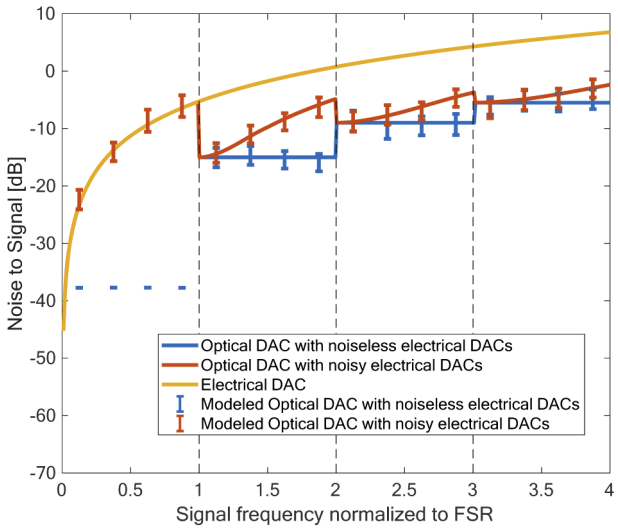

Fig. 12. Noise-to-signal ratio of the optically enabled, spectrally-sliced DAC as a function of the synthesized signal frequency. The analytical model given by Eq. (25) is overlaid with the results from numerical simulations, with 3σ confidence intervals shown with error bars. Three scenarios are shown corresponding to a conventional DAC architecture with electric phase noise only (yellow), an optically enabled DAC with MLL jitter only (blue), and an optically enabled DAC with both electrical and optical phase noise (red).

6. Discussion

The noise model derived and validated in Section 4 can be used to evaluate the ENOB achievable by the spectrally-sliced ADC, as fundamentally limited by oscillator jitter. Assuming four 30 GHz spectral slices, the highest signal frequency that can be digitized is ~120 GHz, which corresponds to an optical side-band to be recorded in the slice with index $m = 3$ and to be transduced to an electric signal with angular frequency $\omega_{RF} - m\omega_r = 2\pi \cdot 30$ GHz digitized by the slice's electrical ADC. A 120 GHz signal frequency is the worst case, as system level noise has then worst sensitivity to both MLL and electric oscillator jitter. Following Eq. (21), the jitter of the electric oscillator, in the order of 6.4 fs, will be applied to the residual $2\pi \cdot 30$ GHz angular frequency, while the jitter of the MLL will be applied to the $m\omega_r = 2\pi \cdot 90$ GHz corresponding to using the fourth slice. Consequently, ADC performance will be mainly limited by electrical jitter once the MLL jitter is significantly below one third of the electric oscillator's, which is true for both the Er-doped fiber and Ti:sapphire lasers discussed in Section 2. I.e., for both MLLs, an ENOB of 9.4, as limited by the electric oscillator jitter, would be achievable, corresponding to an improvement of 2 effective bits relative to a fully electrical architecture, limited to an ENOB of 7.4 for the assumed Δt_e. All reported ENOBs are based on the jitter levels resulting from

Optics EXPRESS

integrating the phase noise between 100 Hz and 10 MHz. The inverse of the SNR and ENOB are shown in Fig. 13 as a function of signal frequency. Figure 13(b) corresponds to the commonly used Walden plot.

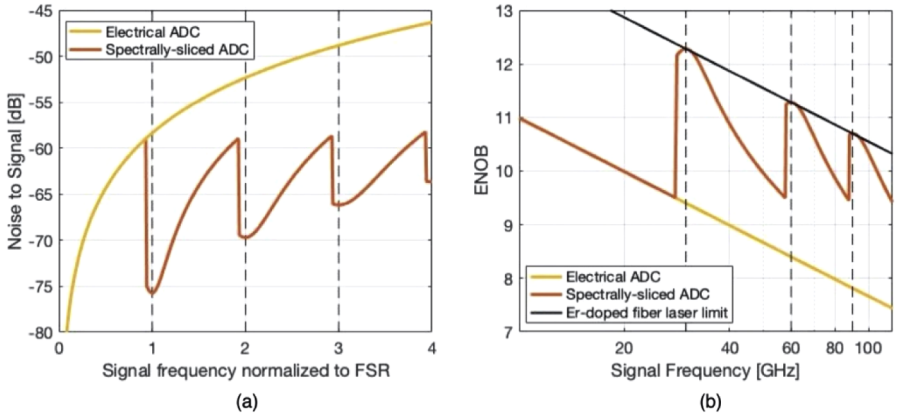

Fig. 13. Noise-to-signal ratio (a) and ENOB (b) of the spectrally-sliced ADC as a function of the RF input signal frequency as predicted by Eq. (21), assuming the 870 attoseconds as jitter of the Er-doped fiber laser (red). The performance of an electrical ADC (yellow) and the limit as constrained by MLL jitter (black) are also shown for reference. The latter corresponds to the performance that would be obtained in the limit of a very large number of slices.

To fully leverage the low jitter of the MLLs, the 120 GHz range would have to be subdivided into many more slices. For example, in order for the effect of electrical jitter to be reduced to the point of being of equal magnitude to that of the 870 attoseconds as of an Er-doped fiber laser, eight 15 GHz slices would be necessary, resulting in an ENOB of 9.9 very close to the best possible 10.3 ENOB limited by the MLL jitter. While using a best-in-class Ti:sapphire laser would in principle result in ENOBs as high as 19, ignoring other noise sources, reaching these performance levels would require in the order of 3,600 slices which appears hardly practical due to the large amount of required hardware and the complexity of the signal processing. Thus, for such low MLL jitter, one may assume the system performance to remain limited by electric oscillator jitter, with the resulting ENOB being driven by the number of implemented slices. Increasing the ENOB by an extra bit to 11 would for example require 12 slices, which already seems quite an engineering challenge. The same scaling limitation applies to time-interleaved ADCs: The maximum frequency digitized by electrical ADCs in each slice scales here too as the maximum signal frequency divided by the number of slices, resulting in the same fundamental ENOB limitation.

7. Conclusions and outlook

Optically enabled, spectrally-sliced ADC and DAC architectures have been analyzed in detail in view of their system level performance in presence of electrical and optical phase noise. System level performance has been derived with analytical formulas and compared against simulation results from comprehensive numerical models. In both architectures, the jitter of the MLL pulse train is shown to be the fundamental aperture-jitter performance limitation. Optical phase noise associated to the central comb line (the correlated phase noise) as well as to other optical carriers plays a secondary role and can be addressed by proper system design and the implementation of compensation mechanisms.

Optics EXPRESS

This work confirms that spectrally-sliced architectures can leverage the full potential of low jitter MLLs and gives guidelines on how to avoid issues with other phase noise sources. For a 4-slice, 120 GHz optically enabled ADC as currently being developed with silicon photonics, the ENOB can be improved by 2 bits relative to a fully electrical architecture relying on an OCXO. Further improvement is possible, but will require increasing the number of slices for a fixed overall system bandwidth, resulting in growing system complexity.

Funding

Deutsche Forschungsgemeinschaft (650602 (PACE)); European Research Council (773248 (TeraSHAPE)).

Disclosures

The authors declare no conflicts of interest.

References

1. W. Kester, Tutorial MT-007 "Aperture Time, Aperture Jitter, Aperture Delay Time – Removing the Confusion" (Analog Devices, 2008).
2. Datasheet, "Ultra Low Phase Noise Oven Controlled Crystal Oscillator OX-305 at 100 MHz" (Vectron International, 2019).
3. Application Notes, "Measurement Considerations for Generating and Analyzing Millimeter-Wave Signals" (Keysight Technologies, 2014).
4. D. G. Santiago and G. J. Dick, "Microwave frequency discriminator with a cooled sapphire resonator for ultra-low phase noise," in *Proc. IEEE Frequency Control Symp.*, 176–182 (1992).
5. R. C. Taber and C. A. Flory, "Microwave Oscillators Incorporating Cryogenic Sapphire Dielectric Resonators," IEEE Trans. Ultrason., Ferroelect., Freq. Contr. **42**(1), 111–119 (1995).
6. E. N. Ivanov and M. E. Tobar, "Low phase-noise sapphire crystal microwave oscillators: current status," IEEE Trans. Ultrason., Ferroelect., Freq. Contr. **56**(2), 263–269 (2009).
7. A. J. Benedick, J. G. Fujimoto, and F. X. Kärtner, "Optical flywheels with attosecond jitter," Nat. Photonics **6**(2), 97–100 (2012).
8. A. Khilo, S. J. Spector, M. E. Grein, A. H. Nejadmalayeri, C. W. Holzwarth, M. Y. Sander, M. S. Dahlem, M. Y. Peng, M. W. Geis, N. A. DiLello, J. U. Yoon, A. Motamedi, J. S. Orcutt, J. P. Wang, C. M. Sorace-Agaskar, M. A. Popović, J. Sun, G.-R. Zhou, H. Byun, J. Chen, J. L. Hoyt, H. I. Smith, R. J. Ram, M. Perrott, T. M. Lyszczarz, E. P. Ippen, and F. X. Kärtner, "Photonic ADC: overcoming the bottleneck of electronic jitter," Opt. Express **20**(4), 4454–4469 (2012).
9. M.-T. Choi, J.-M. Kim, W. Lee, and P. J. Delfyett, "Ultralow noise optical pulse generation in an actively mode-locked quantum-dot semiconductor laser," Appl. Phys. Lett. **88**(13), 131106 (2006).
10. S. Srinivasan, A. Arrighi, M. J. R. Heck, J. Hutchinson, E. Norberg, G. Fish, and J. E. Bowers, "Harmonically Mode-Locked Hybrid Silicon Laser With Intra-Cavity Filter to Suppress Supermode Noise," IEEE J. Sel. Top. Quantum Electron. **20**(4), 8–15 (2014).
11. Z. Wang, K. Van Gasse, V. Moskalenko, S. Latkowski, E. Bente, B. Kuyken, and G. Roelkens, "A III-V-on-Si ultra-dense comb laser," Light: Sci. Appl. **6**(5), e16260 (2017).
12. S. Liu, T. Komljenojic, S. Srinivasan, E. Norberg, G. Fish, and J. E. Bowers, "Characterization of a fully integrated heterogeneous silicon/III-V colliding pulse mode-locked laser with on-chip feedback," Opt. Express **26**(8), 9714–9723 (2018).
13. J. Hauck, A. Zazzi, A. Garreau, F. Lelarge, A. Moscoso-Mártir, F. Merget, and J. Witzens, "Semiconductor Laser Mode Locking Stabilization With Optical Feedback From a Silicon PIC," J. Lightwave Technol. **37**(14), 3483–3494 (2019).
14. K. Shtyrkova, P. T. Callahan, N. Li, E. S. Magden, A. Ruocco, D. Vermeulen, F. X. Kärtner, M. R. Watts, and E. P. Ippen, "Integrated CMOS-compatible Q-switched mode-locked lasers at 1900nm with an on-chip artificial saturable absorber," Opt. Express **27**(3), 3542–3556 (2019).
15. G. C. Valley, "Photonic analog-to-digital converters," Opt. Express **15**(5), 1955–1982 (2007).
16. S. Gupta and B. Jalali, "Time stretch enhanced recording oscilloscope," Appl. Phys. Lett. **94**(4), 041105 (2009).
17. G. Gao and L. Lei, "Photonics-Based Broadband RF Spectrum Measurement With Sliced Coherent Detection and Spectrum Stitching Technique," IEEE Photonics J. **9**(5), 5503111 (2017).
18. R. Schmogrow, M. Winter, M. Meyer, D. Hillerkuss, S. Wolf, B. Bauerle, A. Ludwig, B. Nebendahl, S. Ben-Ezra, J. Meyer, M. Dreschmann, M. Huebner, J. Becker, C. Koos, W. Freude, and J. Leuthold, "Real-time Nyquist pulse generation beyond 100 Gbit/s and its relation to OFDM," Opt. Express **20**(1), 317–337 (2012).
19. C. Schmidt, C. Kottke, V. Jungnickel, and R. Freund, "High-Speed Digital-to-Analog Converter Concepts," Proc. SPIE **10130**, 101300N (2017).

Optics EXPRESS

20. K. Schuh, F. Buchali, W. Idler, Q. Hu, W. Templ, A. Bielik, L. Altenhain, H. Langenhagen, J. Rupeter, U. Duemler, T. Ellermeyer, R. Schmid, and M. Moeller, "100 GSa/s BiCMOS DAC supporting 400 Gb/s dual channel transmission," in *Proc. Europ. Conf. & Exhibit. Opt. Comm. (ECOC)*, 37–39 (2016).
21. L. Alloatti, R. Palmer, S. Diebold, K. P. Pahl, B. Chen, R. Dinu, M. Fournier, J.-M. Fedeli, T. Zwick, W. Freude, C. Koos, and J. Leuthold, "100 GHz silicon-organic hybrid modulator," Light: Sci. Appl. **3**(5), e173 (2014).
22. C. Hoessbacher, A. Josten, B. Baeuerle, Y. Fedoryshyn, H. Hettrich, Y. Salamin, W. Heni, C. Haffner, C. Kaiser, R. Schmid, D. L. Elder, D. Hillerkuss, M. Möller, L. R. Dalton, and J. Leuthold, "Plasmonic modulator with >170 GHz bandwidth demonstrated at 100 GBd NRZ," Opt. Express **25**(3), 1762–1768 (2017).
23. S. Ummethala, T. Harter, K. Koehnle, Z. Li, S. Muehlbrandt, Y. Kutuvantavida, J. Kemal, P. Marin-Palomo, J. Schaefer, A. Tessmann, S. K. Garlapati, A. Bacher, L. Hahn, M. Walther, T. Zwick, S. Randel, W. Freude, and C. Koos, "THz-to-optical conversion in wireless communications using an ultra-broadband plasmonic modulator," Nat. Photonics **13**(8), 519–524 (2019).
24. C. Wang, M. Zhang, X. Chen, M. Bertrand, A. Shams-Ansari, S. Chandrasekhar, P. Winzer, and M. Loncar, "Integrated lithium niobate electro-optic modulators operating at CMOS-compatible voltages," Nature **562**(7725), 101–104 (2018).
25. A. Yacoubian and P. K. Das, "Digital-to-Analog Conversion Using Electrooptic Modulators," IEEE Photonics Technol. Lett. **15**(1), 117–119 (2003).
26. M. A. Soto, M. Alem, M. A. Shoaie, A. Vedadi, C.-S. Brès, L. Thévenaz, and T. Schneider, "Optical sinc-shaped Nyquist pulses of exceptional quality," Nat. Commun. **4**(1), 2898 (2013).
27. J. Meier and T. Schneider, "Precise, High-Bandwidth Digital-to-Analog Conversion by Optical Sinc-Pulse Sequences," in *Proc. German Microwave Conf.*, 166–169 (2019).
28. T. Yilmaz, C. M. DePriest, T. Turpin, J. H. Abeles, and P. J. Delfyett, "Toward a Photonic Arbitrary Waveform Generator Using a Modelocked External Cavity Semiconductor Laser," IEEE Photonics Technol. Lett. **14**(11), 1608–1610 (2002).
29. F. Xia, M. Rooks, L. Sekaric, and Y. Vlasov, "Ultra-compact high order ring resonator filters using submicron silicon photonic wires for on-chip optical interconnects," Opt. Express **15**(19), 11934–11941 (2007).
30. S. Romero-García, A. Moscoso-Mártir, J. Müller, B. Shen, F. Merget, and J. Witzens, "Wideband multi-stage CROW filters with relaxed fabrication tolerances," Opt. Express **26**(4), 4723–4737 (2018).
31. S. Sharif Azadeh, J. Müller, F. Merget, S. Romero-García, B. Shen, and J. Witzens, "Advances in silicon photonics segmented electrode Mach-Zehnder modulators and peaking enhanced resonant devices," Proc. SPIE **9288**, 928817 (2014).
32. S. Lischke, D. Knoll, D. Wolansky, M. Kroh, A. Peczek, and L. Zimmermann, "High-Speed, High-Responsivity Ge Photodiode with NiSi Contacts for an Advanced Photonic BiCMOS Technology," in *Proc. 14th IEEE Conf. Group IV Photon. (GFP)*, 61–62 (2017).
33. S. Gudyriev, C. Kress, H. Zwickel, J. N. Kemal, S. Lischke, L. Zimmermann, C. Koos, and J. C. Scheytt, "Coherent ePIC Receiver for 64 GBaud QPSK in 0.25 (m Photonic BiCMOS Technology," J. Lightwave Technol. **37**(1), 103–109 (2019).
34. A. Mecozzi, C. Antonelli, and M. Shtaif, "Kramers–Kronig coherent receiver," Optica **3**(11), 1220–1227 (2016).
35. J. Lhermite, D. Sabourdy, A. Desfarges-Berthelemot, V. Kermene, A. Barthelemy, and J.-L. Oudar, "Tunable high-repetition-rate fiber lasers for the generation of pulse trains and packets," Opt. Lett. **32**(12), 1734–1736 (2007).
36. D. Mao, X. Liu, Z. Sun, H. Lu, D. Han, G. Wang, and F. Wang, "Flexible high-repetition-rate ultrafast fiber laser," Sci. Rep. **3**(1), 3223 (2013).
37. T. K. Kim, Y. Song, K. Jung, C. Kim, H. Kim, C. H. Nam, and J. Kim, "Sub-100-as timing jitter optical pulse trains from mode-locked Er-fiber lasers," Opt. Lett. **36**(22), 4443–4445 (2011).
38. Datasheet, "E8257D Microwave Analog Signal Generator" (Keysight, 2017).
39. R. Rosales, K. Merghem, A. Martinez, F. Lelarge, A. Accard, and A. Ramdane, "Timing jitter from the optical spectrum in semiconductor passively mode locked lasers," Opt. Express **20**(8), 9151–9160 (2012).
40. R. Rosales, S. G. Murdoch, R. T. Watts, K. Merghem, A. Martinez, F. Lelarge, A. Accard, L. P. Barry, and A. Ramdane, "High performance mode locking characteristics of single section quantum dash lasers," Opt. Express **20**(8), 8649–8657 (2012).
41. R. Paschotta, A. Schlatter, S. C. Zeller, H. R. Telle, and U. Keller, "Optical phase noise and carrier-envelope offset noise of mode-locked lasers," Appl. Phys. B **82**(2), 265–273 (2006).
42. S. Diez, C. Schmidt, R. Ludwig, H. G. Weber, K. Obermann, S. Kindt, I. Koltchanov, and K. Petermann, "Four-Wave Mixing in Semiconductor Optical Amplifiers for Frequency Conversion and Fast Optical Switching," IEEE J. Sel. Top. Quantum Electron. **3**(5), 1131–1145 (1997).
43. F. Kefelian, S. O'Donoghue, M. T. Todaro, J. G. McInerney, and G. Huyet, "RF Linewidth in Monolithic Passively Mode-Locked Semiconductor Laser," IEEE Photonics Technol. Lett. **20**(16), 1405–1407 (2008).
44. G. Di Domenico, S. Schilt, and P. Thomann, "Simple approach to the relation between laser frequency noise and laser line shape," Appl. Opt. **49**(25), 4801–4807 (2010).
45. M. Bahmanian, J. Tiedau, C. Silberhorn, and J. C. Scheytt, "Octave-Band Microwave Frequency Synthesizer Using Mode-Locked Laser as a Reference," in *Proc. of 2019 Int. Top. Meet. on Microwave Photon. (MWP)*.